

Flutter Prediction Using Reduced-Order Modeling

Brandon M. Lowe* and David W. Zingg†
Institute for Aerospace Studies, University of Toronto,
4925 Dufferin St, Toronto, Ontario, M3H 5T6, Canada

Typical aerodynamic shape and multidisciplinary optimization algorithms omit high-fidelity flutter predictions due to the associated computational costs. This paper presents a model order reduction framework as a step towards flutter constrained aircraft optimization. The Euler equations linearized about a steady-state solution are used as the governing unsteady flow equations. Using proper orthogonal decomposition, a reduced basis is constructed onto which the governing equations are projected. The result is a linear reduced-order model (ROM) with significantly fewer degrees of freedom capable of rapidly approximating aerodynamic forces. This ROM is coupled to a linear structural model to create a single monolithic aeroelastic system. The eigenvalues of the resulting system are analyzed for various flow conditions to determine the onset of flutter in the system. The flutter boundaries obtained for both a two degree of freedom airfoil structure and the AGARD 445.6 wing model show good agreement with the full-order model and with the literature.

I. Introduction

IN recent years, a strong emphasis has been placed on the need for increased aircraft fuel efficiency. Ambitious fuel burn reduction goals, such as those set by NASA's N+3 efforts, require a shift towards novel aircraft designs. Such efficient designs can be conceptualized with the aid of aerodynamic shape and multidisciplinary optimization tools based on high-fidelity computational fluid dynamics (CFD) [1–4]. Historically, due to complexity and computational costs, flutter constraints have often been omitted from such tools. Thus, resulting optimal aircraft geometries could potentially be subject to this dangerous aeroelastic phenomenon.

Recently, the inclusion of flutter constraints in both aerodynamic and structural optimization has gained traction. Mallik *et al.* [5] studied the effects of a flutter constraint on the multidisciplinary optimization (MDO) of a truss-braced-wing aircraft. Using a modified version of Theodorsen's linear aerodynamic function [6], they showed that inclusion of a flutter constraint lead to meaningful penalties on both the weight and fuel efficiency of the resulting aircraft. Jonsson *et al.* [7] have formulated a flutter constraint based on tracking the aeroelastic modes from the *pk* method, and aggregated the constraints on all modes using the Kreisselmeier-Steinhauser function. In their work, aerodynamic forces were approximated using a doublet lattice method (DLM). Lupp and Cesnik [8] have extended this method to include geometric nonlinearities, similarly relying on linear aerodynamic methods. A low-order aerodynamic model has been implemented into an aircraft design tool by Opgenoord *et al.* [9]. This aerodynamic model is calibrated using high-fidelity CFD simulations and was originally formulated in two-dimensions but has been extended to three-dimensions using aerodynamic strip theory. Jacobson *et al.* [10] have developed a method to predict flutter based on transient responses from a structural model coupled to a high-fidelity flow solver. Using the matrix pencil method, they approximate the damping of the aeroelastic response to a structural excitation for a given dynamic pressure and use an optimization approach to modify the dynamic pressure until the flutter boundary is determined. For further information on flutter-based constraints for aircraft optimization, see the excellent review by Jonsson *et al.* [11].

Linear aerodynamic methods (such as DLM) have been widely used for flutter predictions in the past due to their low computational cost. However, these methods fail to model nonlinear flow features accurately in the transonic regime important for modern commercial aircraft [12]. This lack of accuracy has led to overly conservative aircraft designs [13], and hence losses in potential fuel savings. Alternatively, high-fidelity CFD presents a means to model aerodynamics accurately for dynamic aeroelastic analysis. In reality, however, due in part to the unsteady nature of the problem, the large number of degrees of freedom, and the number of flight conditions to consider, the use of CFD for flutter predictions in a design context remains intractable. This problem is exacerbated when introducing flutter predictions

*PhD Candidate, University of Toronto, brandon.lowe@mail.utoronto.ca

†University of Toronto Distinguished Professor of Computational Aerodynamics and Sustainable Aviation, Director, Centre for Research in Sustainable Aviation, dwz@oddjob.utias.utoronto.ca

into an aerodynamic shape optimization framework, for which each new iteration of aircraft geometry requires a fresh flutter analysis.

Model order reduction of dynamical systems has reached significant maturity. These methods aim to generate reduced-order models (ROMs) which accurately capture the dynamic behaviour of the full-order system in a fraction of the computational time. ROMs have previously been used for dynamic aeroelastic analysis [14–24]. Among these examples, projection-based ROMs with reduced bases constructed using proper orthogonal decomposition (POD) have been widely used. Notably, Thomas *et al.* [14] were among the first to use a POD-based ROM for aeroelastic modeling. Using the linearized Euler equations in the frequency domain, they constructed ROMs which provided flutter boundaries with good agreement to full-order methods. Beran *et al.* [15] used a POD-based ROM to predict the onset of limit-cycle oscillations for a nonlinear panel in a two-dimensional flow. A few years later, Lieu *et al.* [17, 18] modelled the dynamic aeroelastic behaviour of a complete aircraft configuration using a POD-based ROM constructed from the frequency domain linearized Euler equations. More recently, Amsallem *et al.* [19] used the same governing flow equations to predict the flutter boundary of a wing-store configuration using a parameterized ROM. Through an interpolation framework, they were capable of quickly adapting the aerodynamic ROM for various Mach numbers.

This paper presents a model order reduction approach for flutter predictions as a step towards an aircraft optimization constraint. In this approach, the time-domain linearized discrete Euler equations are used to model the unsteady aerodynamics. Linear projection-based model order reduction is used to reduce the dimension of the governing flow model by several orders of magnitude. The resulting aerodynamic ROM is coupled to the structural model to form a single monolithic system. The eigenvalues of this system are analyzed to determine the onset of flutter. Two example cases are presented: a two degree of freedom airfoil structure capable of pitching and plunging, and the well known AGARD 445.6 wing flutter test case.

II. Flow Solver

This section presents an overview of the nonlinear flow solver developed at the University of Toronto used in this work to obtain steady-state flow solutions. Subsequently, the linearized discrete Euler equations are derived. Mesh deformation and time-marching methodologies are also presented. For ease of presentation, certain quantities associated to the aerodynamic model are indicated with the subscript a , whereas analogous values for the structural models will be presented with a subscript s .

A. Nonlinear Flow Solver

The steady-state flow solutions for this work are obtained using a multiblock structured finite-difference flow solver for the Euler equations developed by Hicken and Zingg [25]. Spatial discretization is achieved using second-order-accurate summation-by-parts operators, while boundary conditions are weakly imposed using simultaneous-approximation terms. The discrete flow equations are solved iteratively using Newton’s method. At each Newton iteration, the linear system is solved inexactly using the Krylov-subspace algorithm FGMRES with an approximate Schur preconditioner [26].

B. Linearized Discrete Euler Equations

In this section, the Euler equations are linearized after discretization in space. Transforming the Euler equations to computational space, and subsequently discretizing in space results in the following set of N_a ordinary differential equations,

$$\frac{d(J^{-1}\mathbf{q})}{dt} + \mathbf{R}(\mathbf{q}, \mathbf{x}, \dot{\mathbf{x}}) = 0, \quad (1)$$

where $\mathbf{q} \in \mathbb{R}^{N_a}$ is the vector of conservative flow states at each node, $\mathbf{R} \in \mathbb{R}^{N_a}$ is the residual vector, and $J^{-1} \in \mathbb{R}^{N_a \times N_a}$ is a diagonal matrix of inverse metric Jacobians of the transformation to curvilinear coordinates. The equations are linearized with respect to the conservative flow state \mathbf{q} , the grid node coordinates \mathbf{x} , and the grid node velocities $\dot{\mathbf{x}}$. Fluctuations of the latter two quantities will serve as inputs into the system of equations and will be obtained from the structural model. As the linearization is about a nonlinear steady-state, important nonlinear effects, such as small shock wave motion, are captured [27].

The time-derivative term in (1) is first put into non-conservative form,

$$\frac{d(J^{-1}\mathbf{q})}{dt} = J^{-1}\dot{\mathbf{q}} + \frac{dJ^{-1}}{dt}\mathbf{q}, \quad (2)$$

where a dot above a quantity represents a derivative in time. Based on the geometric conservation law (GCL), first proposed by Thomas and Lombard [28], the term $\frac{dJ^{-1}}{dt}$ can be expressed as

$$\frac{dJ^{-1}}{dt} = - \left(\frac{d\hat{\xi}_t}{d\xi} + \frac{d\hat{\eta}_t}{d\eta} + \frac{d\hat{\zeta}_t}{d\zeta} \right), \quad (3)$$

where ξ, η, ζ are curvilinear coordinates, and $\hat{\xi}_t, \hat{\eta}_t, \hat{\zeta}_t$ are the time metric terms. The time metrics are dependent on both grid coordinates and velocities and can be expanded with respect to these quantities in a Taylor series about a steady-state. However, at steady-state the grid velocity is zero; therefore any first-order dependence on the grid coordinates disappears. Thus, expanding both terms in (2) in a Taylor series about the steady-state and omitting second-order terms gives

$$\frac{d(J^{-1}\mathbf{q})}{dt} \approx J_0^{-1}\delta\dot{\mathbf{q}} + \frac{\partial}{\partial\dot{\mathbf{x}}} \left(\frac{dJ^{-1}}{dt} \right) \mathbf{q}_0\delta\dot{\mathbf{x}}, \quad (4)$$

where steady-state quantities are denoted with a subscript 0, and fluctuating quantities with a δ . Similarly, the residual in (1) is expanded in a Taylor series such that

$$\mathbf{R}(\mathbf{q}, \mathbf{x}, \dot{\mathbf{x}}) \approx \mathbf{R}(\mathbf{q}_0, \mathbf{x}_0, \dot{\mathbf{x}}_0) + \frac{\partial\mathbf{R}}{\partial\mathbf{q}}\delta\mathbf{q} + \frac{\partial\mathbf{R}}{\partial\mathbf{x}}\delta\mathbf{x} + \frac{\partial\mathbf{R}}{\partial\dot{\mathbf{x}}}\delta\dot{\mathbf{x}}, \quad (5)$$

where the residual of the steady problem, $\mathbf{R}(\mathbf{q}_0, \mathbf{x}_0, \dot{\mathbf{x}}_0)$, is zero. Combining equations (4) and (5) provides the linearized discrete Euler equations:

$$J_0^{-1}\delta\dot{\mathbf{q}} + \frac{\partial\mathbf{R}}{\partial\mathbf{q}}\delta\mathbf{q} + \frac{\partial\mathbf{R}}{\partial\mathbf{x}}\delta\mathbf{x} + \left(\frac{\partial}{\partial\dot{\mathbf{x}}} \left(\frac{dJ^{-1}}{dt} \right) \mathbf{q}_0 + \frac{\partial\mathbf{R}}{\partial\dot{\mathbf{x}}} \right) \delta\dot{\mathbf{x}} = 0. \quad (6)$$

For aeroelastic considerations, the outputs of interest are the aerodynamic force fluctuations about a steady-state. Forces are computed using the aerodynamic pressure, which is explicitly dependent on the flow state \mathbf{q} , and the area-weighted surface normal, which is explicitly dependent on the grid node coordinates \mathbf{x} . Expanding the fluctuations of the force as a Taylor series, one obtains

$$\delta\mathbf{f}_a \approx \frac{\partial\mathbf{f}_a}{\partial\mathbf{q}}\delta\mathbf{q} + \frac{\partial\mathbf{f}_a}{\partial\mathbf{x}}\delta\mathbf{x}. \quad (7)$$

Combining equations (6) and (7) provides the complete linear time-invariant (LTI) system describing the evolution and output of the aerodynamic model. Introducing the input vector as $\mathbf{x}_a = [\delta\dot{\mathbf{x}}^T, \delta\mathbf{x}^T]^T$ and dropping the δ 's from the vectors \mathbf{q} and \mathbf{f}_a to simplify the notation, the LTI system is

$$\begin{aligned} E\dot{\mathbf{q}} &= A\mathbf{q} + \tilde{B}\mathbf{x}_a, \\ \mathbf{f}_a &= C\mathbf{q} + \tilde{D}\mathbf{x}_a. \end{aligned} \quad (8)$$

From the linearization above, the system matrices are,

$$A = \frac{\partial\mathbf{R}}{\partial\mathbf{q}}, \quad \tilde{B} = \left[\left(\frac{\partial}{\partial\dot{\mathbf{x}}} \left(\frac{dJ^{-1}}{dt} \right) \mathbf{q}_0 + \frac{\partial\mathbf{R}}{\partial\dot{\mathbf{x}}} \right) \quad \frac{\partial\mathbf{R}}{\partial\dot{\mathbf{x}}} \right], \quad C = \frac{\partial\mathbf{f}_a}{\partial\mathbf{q}}, \quad \tilde{D} = \left[0 \quad \frac{\partial\mathbf{f}_a}{\partial\mathbf{x}} \right], \quad E = J_0^{-1}.$$

C. Algebraic Mesh Deformation

In the formulation of equation (8), the vectors $\delta\mathbf{x}$ and $\delta\dot{\mathbf{x}}$ in the input vector \mathbf{x}_a denote the fluctuating node coordinates and velocities of the entire computational grid, also known as the volume grid. A typical volume grid can easily contain $\mathcal{O}(10^5)$ nodes, leading to a large input vector \mathbf{x}_a . Such a vector leads to a large number of operations for its respective matrix-vector product in equation (8); therefore reducing the size of this vector would save on both memory and computational expense. Consider a linear mesh deformation algorithm which can be cast in the following form

$$\delta\mathbf{x} = K_m\delta\mathbf{x}_{\text{surf}}, \quad (9)$$

where $\delta\mathbf{x}$ is the vector of volume node displacements, $\delta\mathbf{x}_{\text{surf}}$ the vector of surface node displacements, and K_m the mesh deformation matrix. If K_m is time-invariant, then one can also relate the volume node velocity fluctuations to the surface node velocity fluctuations by

$$\delta\dot{\mathbf{x}} = K_m \delta\dot{\mathbf{x}}_{\text{surf}}. \quad (10)$$

The matrix K_m can be integrated into the linearized Euler equations as a precomputing step, reducing the overall number of inputs into the system. To see this, denote the new input matrices B and D as

$$B = \tilde{B} \begin{bmatrix} K_m & 0 \\ 0 & K_m \end{bmatrix}, \quad D = \tilde{D} \begin{bmatrix} K_m & 0 \\ 0 & K_m \end{bmatrix}, \quad (11)$$

and the new input vector as $\mathbf{x}_{a,\text{surf}} = [\delta\dot{\mathbf{x}}_{\text{surf}}^T, \delta\mathbf{x}_{\text{surf}}^T]^T$. Equation (8) simply becomes

$$\begin{aligned} E\dot{\mathbf{q}} &= A\mathbf{q} + B\mathbf{x}_{a,\text{surf}}, \\ \mathbf{f}_a &= C\mathbf{q} + D\mathbf{x}_{a,\text{surf}}. \end{aligned} \quad (12)$$

For this work, the matrix K_m is constructed based on an algebraic mesh deformation algorithm described by Leung and Zingg [29]. In this algorithm, the movement of the k^{th} volume node is given by the equation

$$\delta x_k = \frac{\delta x_{k,\text{surf}}}{2} (1 + \cos(\pi S_k)), \quad (13)$$

where $\delta x_{k,\text{surf}}$ is the displacement of the surface node on the same grid line, and S_k is the normalized arc length from the surface node to the k^{th} volume node. Algebraic mesh deformation has not been found to be robust for large surface movements and may lead to poor mesh quality as a result. However, the use of the linearized Euler equations is limited to small surface movements; thus algebraic mesh deformation is sufficient.

D. Time Marching

As will be discussed in the following section, the full-order linearized Euler equations (12) are marched in time in order to create a reduced basis onto which the equations are projected. The second-order backwards difference method is used to march the equations in time. At each time step, the linear system is solved using the Krylov solver GCROT(m, k) [30] with an approximate Schur preconditioner [26].

III. Model Order Reduction

The LTI system (12) retains the same dimension as the original nonlinear discrete governing flow equations and thus remains impractical for fast flutter predictions. In order to reduce computational expense, a projection-based model order reduction approach is used for which the reduced basis is created using POD. Excellent literature exists on the fundamentals and applications of POD [31–34]. To keep this paper self contained, the general concepts are reviewed briefly in this section. Subsequently, the procedure for snapshot collection is discussed.

A. POD-based Model Order Reduction

The key goal of POD is to represent a set of data with as few basis vectors as possible. To this end, consider a set of m state (or “snapshot”) vectors $\mathbf{q}_1, \mathbf{q}_2, \dots, \mathbf{q}_m \in \mathbb{R}^{N_a}$ at different instants in time, that is $\mathbf{q}_j = \mathbf{q}(t_j)$. We wish to create a set of orthogonal basis vectors $\boldsymbol{\phi}_i \in \mathbb{R}^{N_a}$ which minimizes the least squares error of the snapshot reconstruction. This is done by solving the eigenproblem [32]:

$$WSS^T W\boldsymbol{\phi}_i = \lambda_i W\boldsymbol{\phi}_i, \quad (14)$$

where $S \in \mathbb{R}^{N_a \times m}$ is the snapshot matrix containing the m snapshots stored column-wise, $W \in \mathbb{R}^{N_a \times N_a}$ is a symmetric positive-definite matrix which defines a weighted inner product in Euclidean space, and λ_i is the eigenvalue associated to the i^{th} eigenvector $\boldsymbol{\phi}_i$. The weighted inner product matrix W may serve multiple purposes, including as an approximation to an inner product in continuous space (for example an L^2 inner product) [32], and as an inner product which ensures the stability of the resulting ROM [35]. The reduced basis $\Phi \in \mathbb{R}^{N_a \times r_a}$ onto which the governing equations are projected, is formed such that $\Phi = [\boldsymbol{\phi}_1, \boldsymbol{\phi}_2, \dots, \boldsymbol{\phi}_{r_a}]$ with the eigenvectors and values arranged as $\lambda_1 \geq \lambda_2 \geq \dots \geq \lambda_m$ and $r_a \leq m$.

The sum of the eigenvalues associated to the excluded eigenvectors quantifies the snapshot reconstruction error,

$$\sum_{j=1}^m \|\mathbf{q}_j - \sum_{i=1}^{r_a} (\mathbf{q}_j^T \mathbf{W} \boldsymbol{\phi}_i) \boldsymbol{\phi}_i\|_W^2 = \sum_{j=r_a+1}^m \lambda_j, \quad (15)$$

where $\|\boldsymbol{\psi}\|_W = \sqrt{\boldsymbol{\psi}^T \mathbf{W} \boldsymbol{\psi}}$ is the induced norm associated to \mathbf{W} . This can be used as a metric to choose an appropriate reduced basis dimension r_a . With a tolerance η (often smaller than 10^{-1}), one can compute the smallest r_a such that

$$1 - \frac{\sum_{i=1}^{r_a} \lambda_i}{\sum_{i=1}^m \lambda_i} \leq \eta. \quad (16)$$

For further details, see [31, 32, 34].

In projecting equation (12) onto the reduced basis, one approximates the evolution of the solution in the reduced space [31]:

$$\mathbf{q}(t) \approx \boldsymbol{\Phi} \mathbf{u}_a(t), \quad (17)$$

where $\mathbf{u}_a \in \mathbb{R}^{r_a}$ is a vector of time-dependent coefficients. This approximation results in the residual $\mathbf{R}_{ROM} = \mathbf{E} \boldsymbol{\Phi} \mathbf{u}_a - \mathbf{A} \boldsymbol{\Phi} \mathbf{u}_a - \mathbf{B} \mathbf{x}_{a,\text{surf}}$. Enforcing the Galerkin condition, which states that the residual is orthogonal to the reduced space

$$\boldsymbol{\Phi}^T \mathbf{W} \mathbf{R}_{ROM} = 0, \quad (18)$$

gives the ROM of interest,

$$\begin{aligned} E_r \dot{\mathbf{u}}_a &= A_r \mathbf{u}_a + B_r \mathbf{x}_{a,\text{surf}}, \\ f_{a,r} &= C_r \mathbf{u}_a + D_r \mathbf{x}_{a,\text{surf}}. \end{aligned} \quad (19)$$

This ROM contains r_a degrees of freedom, with $r_a \ll N_a$. The reduced matrices are:

$$A_r = \boldsymbol{\Phi}^T \mathbf{W} \mathbf{A} \boldsymbol{\Phi}, \quad B_r = \boldsymbol{\Phi}^T \mathbf{W} \mathbf{B}, \quad C_r = \mathbf{C} \boldsymbol{\Phi}, \quad D_r = \mathbf{D}, \quad E_r = \boldsymbol{\Phi}^T \mathbf{W} \mathbf{E} \boldsymbol{\Phi}. \quad (20)$$

B. Snapshot Collection

Snapshots are collected using a simultaneous input excitation method, similar to the approaches detailed in [36, 37]. As the name suggests, all inputs for the aerodynamic model are excited simultaneously during a single flow solve, and the resulting flow field at each time instance is stored as a snapshot and used later to create the POD-based reduced basis. The use of simultaneous excitations for snapshot collection has been found to be more economical in terms of computational time when generating the ROM compared to exciting each system input in separate flow simulations [36]. One key aspect is that each input signal must be relatively uncorrelated to generate a rich database of flow field reactions. This was attained by using filtered noise for the excitation of each system input.

For the system of interest (12), the input vector $\mathbf{x}_{a,\text{surf}}$ includes both structural velocities and displacements. As will be discussed in the following section, a modal representation of the structure is used in this work. Thus, each input in equation (12) is associated to a structural mode shape, each mode shape itself being associated to a natural frequency. In collecting snapshots for the aerodynamic model, it has been found that ROMs capable of accurate flutter predictions are obtained by exciting the structural mode shapes using filtered noise. Specifically, the noise is filtered through a low-pass filter with a cutoff frequency close to the natural frequency of each mode shape (scaled according to some reference dynamic pressure). Figure 1 shows an example of excitations provided to the first four inputs for the AGARD 445.6 wing test case. Note the smoothness of the first input's excitations compared to the others, indicative of a lower cutoff frequency due to the lower associated natural frequency.

IV. Aeroelastic Model

To determine the onset of flutter, the aerodynamic ROM (19) is coupled to a structural model to form a complete aeroelastic system. This section first presents the formulation of the structural equations of motion. The displacement and force transfer between the aerodynamic and the structural model is then described. Finally, the coupled monolithic aeroelastic system is presented.

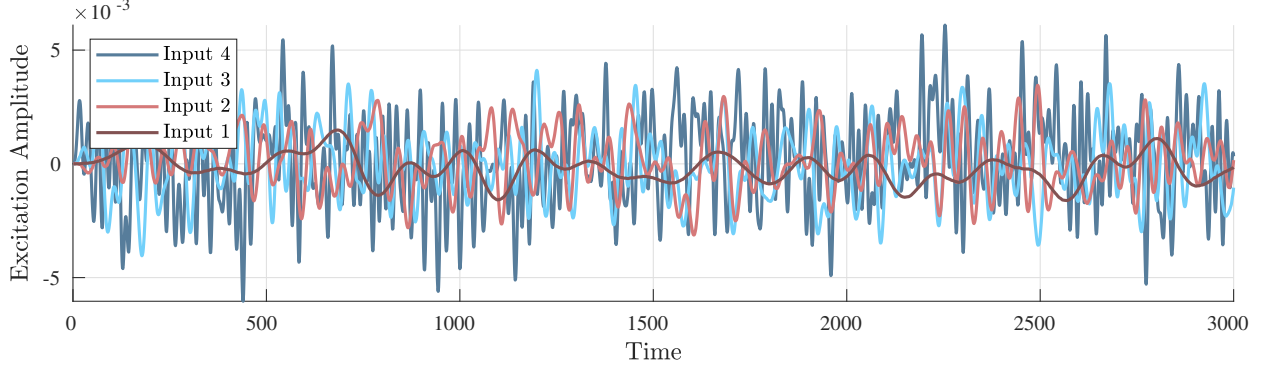


Fig. 1 Example of input excitations for snapshot collection for the AGARD 445.6 wing test case.

A. Structural Model

It is common to model a structure's motion using a modal method [38]. Given a structural model with N_s degrees of freedom, the spatial dependence is described via r_s mode shapes, where $r_s < N_s$. These mode shapes typically correspond to the free vibration modes of the structure, given by the generalized eigenvalue problem

$$K\psi_i = \omega_i^2 M\psi_i, \quad (21)$$

where $K \in \mathbb{R}^{N_s \times N_s}$ is the stiffness matrix, $M \in \mathbb{R}^{N_s \times N_s}$ is the mass matrix, and $\omega_i \in \mathbb{R}$ and $\psi_i \in \mathbb{R}^{N_s}$ are the modal frequency and mode shape associated to the i^{th} free vibration mode. These mode shapes are orthogonal to one another and can be scaled to produce unit modal mass. Using the first r_s modes to model the system and neglecting damping terms gives the following uncoupled equations of motion:

$$\ddot{\mathbf{w}} + \Omega \mathbf{w} = \Psi^T \mathbf{f}. \quad (22)$$

Here, $\mathbf{w} \in \mathbb{R}^{r_s}$ is the vector of generalized displacements for each mode, $\mathbf{f} \in \mathbb{R}^{N_s}$ the vector of applied forces, $\Omega \in \mathbb{R}^{r_s \times r_s}$ the diagonal matrix of squared modal frequencies ω_i^2 , and $\Psi \in \mathbb{R}^{N_s \times r_s}$ the matrix containing the structural mode shapes ψ_i stored column-wise.

In order to couple this system with the aerodynamic ROM (19), it is convenient to rewrite equation (22) as a system of first-order ordinary differential equations. Introducing the new state vector $\mathbf{u}_s = [\dot{\mathbf{w}}^T, \mathbf{w}^T]^T$ leads to the following formulation

$$\dot{\mathbf{u}}_s = A_s \mathbf{u}_s + \mathbf{f}_s, \quad (23)$$

where,

$$A_s = \begin{bmatrix} 0 & -\Omega \\ I & 0 \end{bmatrix}, \quad \mathbf{f}_s = \begin{bmatrix} \Psi^T \mathbf{f} \\ 0 \end{bmatrix}.$$

B. Model Coupling

In coupling the structural model (23) and the aerodynamic ROM (19), two challenges arise. The first comes from the fact that quantities exchanged between models must have common dimensions. The second arises from the non-coinciding surface grids between the two models, resulting in the need for force and displacement transfer between grids. In this section, the variable representing time is t_a for the aerodynamic model and t_s for the structural model. Additionally, for clarity, time derivatives in this section will be denoted not by a dot, but rather by $\frac{d}{dt_a}$ or $\frac{d}{dt_s}$.

1. Dimensional Consistency

To couple the aerodynamic and structural models, quantities which are exchanged must be dimensionally consistent. To this end, the following time and force scaling factors are introduced:

$$t_s = \sigma_t t_a, \quad \mathbf{f}_s = \sigma_f \mathbf{f}_a. \quad (24)$$

Note that f_s and f_a represent only scalar force quantities for the structural and aerodynamic model, respectively. They are not denoted as vectors because the surface grids do not coincide between models; this is addressed in the next subsection.

From the aerodynamic model, dimensional time \tilde{t} and force \tilde{f} are obtained with the following equations:

$$\tilde{t} = \frac{L_{\text{ref}} M_{\infty}}{V_{\infty}} t_a, \quad \tilde{f} = L_{\text{ref}}^2 q_{\infty} f_a, \quad (25)$$

where L_{ref} is a reference length, M_{∞} is the freestream Mach number, V_{∞} is the freestream velocity, and q_{∞} is the freestream dynamic pressure. The structural models presented in this paper each possess different dimensions. For the AGARD 445.6 wing, the model is kept in dimensional form, thus $t_s = \tilde{t}$ and $f_s = \tilde{f}$. Additionally, the aerodynamic grid was constructed around a dimensional AGARD wing geometry, therefore $L_{\text{ref}} = 1$ in. This leads to the following scaling factors:

$$\sigma_t = \frac{L_{\text{ref}} M_{\infty}}{\sqrt{2q_{\infty} \rho_{\infty}}}, \quad \sigma_f = L_{\text{ref}}^2 q_{\infty}, \quad (26)$$

where ρ_{∞} is the freestream density. For the two degree of freedom structural model, time is nondimensionalized by the torsional natural frequency $t_s = \omega_{\alpha} \tilde{t}$, and applied forces are nondimensionalized as $f_s = \tilde{f} / (mb\omega_{\alpha}^2)$, where m is the airfoil mass, and b the semi-chord. Additionally, aerodynamic grid was constructed about an airfoil geometry nondimensionalized by the chord length, therefore the length scaling is $L_{\text{ref}} = 2b$. Using the definition of the two-dimensional mass ratio $\mu = m / (\rho_{\infty} b^2 \pi)$ we get the scaling factors:

$$\sigma_t = \frac{2M_{\infty}}{V_f \sqrt{\mu}}, \quad \sigma_f = \frac{1}{\pi} V_f^2, \quad (27)$$

where the flutter speed index is defined as

$$V_f = \frac{V_{\infty}}{b\omega_{\alpha} \sqrt{\mu}}. \quad (28)$$

2. Displacement and Force Transfer

In general, the fluid grid surface nodes do not coincide with the structural grid surface nodes due to the different nature of model discretizations. Therefore, quantities which must be exchanged between the two models must be transferred. Specifically, the generalized coordinates \mathbf{w} and velocities $\frac{d\mathbf{w}}{dt_s}$ of the structure must be transformed into aerodynamic surface mesh deformations $\delta\mathbf{x}_{\text{surf}}$ and velocities $\frac{d\delta\mathbf{x}_{\text{surf}}}{dt_a}$, respectively. Additionally, the force output from the aerodynamic ROM $f_{a,r}$ must be transformed into f_s , the force applied to the structural model. For this, we introduce the transfer matrices K_s and K_a , and make use of the scaling factors in (24),

$$\delta\mathbf{x}_{\text{surf}} = K_s \mathbf{w}, \quad \frac{d\delta\mathbf{x}_{\text{surf}}}{dt_a} = \sigma_t K_s \frac{d\mathbf{w}}{dt_s}, \quad f_s = \sigma_f K_a f_{a,r}, \quad (29)$$

In the two degree of freedom structural system introduced later in this paper, the matrix K_s is formulated analytically using a small angle approximation, while K_a is formulated based on the equations for C_l and C_m . For more complex geometries, a number of options exist for constructing K_s and K_a . In the present work, Rendall and Allen's radial basis function interpolation [39] is used to construct the transfer matrices for the AGARD 445.6 wing case. The radial basis function approach ensures that energy, and total force and moment are conserved between both models. Moreover, it allows for the exact recovery of translation and rotation. This method is chosen for the aforementioned properties, and for its ease of implementation: it is a point cloud based method and hence no grid connectivity information is required. For further information see [39].

C. Monolithic Aeroelastic System

Recall that $\mathbf{x}_{a,\text{surf}}$ is the input vector for the aerodynamic model (19), composed of two vectors: the aerodynamic surface velocity fluctuations $\frac{d\delta\mathbf{x}_{\text{surf}}}{dt_a}$, and the aerodynamic surface displacement fluctuations $\delta\mathbf{x}_{\text{surf}}$. From equation (29) above, the input vector can be redefined as

$$\mathbf{x}_{a,\text{surf}} = \begin{bmatrix} \frac{d\delta\mathbf{x}_{\text{surf}}}{dt_a} \\ \delta\mathbf{x}_{\text{surf}} \end{bmatrix} = \begin{bmatrix} \sigma_t K_s \frac{d\mathbf{w}}{dt_s} \\ K_s \mathbf{w} \end{bmatrix} = \begin{bmatrix} \sigma_t K_s & 0 \\ 0 & K_s \end{bmatrix} \mathbf{u}_s, \quad (30)$$

Now inserting equation (30) into the aerodynamic model (19), and using (24) gives

$$\begin{aligned}\sigma_t E_r \frac{d\mathbf{u}_a}{dt_s} &= A_r \mathbf{u}_a + \bar{B}_r \mathbf{u}_s, \\ \mathbf{f}_{a,r} &= C_r \mathbf{u}_a + \bar{D}_r \mathbf{u}_s,\end{aligned}\tag{31}$$

where we define

$$\bar{B}_r = B_r \begin{bmatrix} \sigma_t K_s & 0 \\ 0 & K_s \end{bmatrix}, \quad \bar{D}_r = D_r \begin{bmatrix} \sigma_t K_s & 0 \\ 0 & K_s \end{bmatrix}.\tag{32}$$

Next the aerodynamic forces are scaled appropriately; this is done with equation (29). Rewriting the structural model (23) using equation (29) and the aerodynamic force approximation from (31) gives

$$\frac{d\mathbf{u}_s}{dt_s} = (A_s + \sigma_f K_a \bar{D}_r) \mathbf{u}_s + \sigma_f K_a C_r \mathbf{u}_a\tag{33}$$

Finally, there remains only the task of creating the monolithic system from equations (31) and (33),

$$\mathcal{E} \frac{d\mathbf{u}}{dt_s} = \mathcal{A} \mathbf{u},\tag{34}$$

where

$$\mathbf{u} = \begin{bmatrix} \mathbf{u}_s \\ \mathbf{u}_a \end{bmatrix}, \quad \mathcal{E} = \begin{bmatrix} I & 0 \\ 0 & \sigma_t E_r \end{bmatrix}, \quad \mathcal{A} = \begin{bmatrix} A_s + \sigma_f K_a \bar{D}_r & \sigma_f K_a C_r \\ \bar{B}_r & A_r \end{bmatrix},\tag{35}$$

with $I \in \mathbb{R}^{2r_s \times 2r_s}$ as the identity matrix. Note that this system is dependent on the dynamic pressure q_∞ (or the flutter speed index V_f) through the scaling factors σ_t and σ_f . By solving the generalized eigenproblem

$$\mathcal{A} \mathbf{v} = \lambda \mathcal{E} \mathbf{v},\tag{36}$$

for a given dynamic pressure (or flutter speed index), the stability of the system can be determined. The point at which any of the eigenvalues in the system cross the imaginary axis (i.e. gain a positive real value) indicates the onset of flutter.

V. Results

Results from the linearized Euler equations are compared to the nonlinear equations for a transonic pitching airfoil test case. Subsequently, flutter prediction results are presented for a two degree of freedom aeroelastic test case and the AGARD 445.6 wing case. An aeroelastic transient time history comparison between the ROM and the full-order linearized Euler equations is presented for the AGARD wing.

A. Results for the Linearized Discrete Euler Equations

Results are presented to assess the accuracy of the linearized discrete Euler equations for unsteady aerodynamic force approximations. A popular test case for unsteady transonic flow is the pitching NACA 64A010 airfoil at a freestream Mach number of 0.796, for which experimental data is provided by Davis [40]. The airfoil pitches at a reduced frequency ($\omega b/V_\infty$) of 0.202, with a mean incidence of 0° , and a pitching amplitude of $\pm 1.01^\circ$. The case was run using both the nonlinear and linearized Euler equations.

Simulations were run using the implicit Euler time-marching method with a time step size of 0.02 nondimensional time units, equivalent to 977 steps per pitching cycle. This small time step size was chosen to ensure that time-marching errors were negligible. Figure 2 shows the evolution of C_l and C_m , the lift and pitching moment coefficients, as a function of the angle of attack α for the sixth cycle of motion. One can see that, though some error is present, in general the linearized Euler equations are capable of capturing similar behaviour as their nonlinear counterpart for this case. Quantitatively, the maximum difference in C_l and C_m between the linearized and nonlinear equations for the sixth pitching cycle are found to be 1.26% and 6.10%, respectively. From both the computational and experimental results, a shock wave is observed which oscillates about the mid-chord. This indicates that the linearized Euler equations are able to capture some shock wave motion. Discrepancies between the experimental and computational results are attributed, in part, to the absence of shock-boundary-layer interactions due to the use of the Euler equations, as discussed by Chyu *et al.* [41].

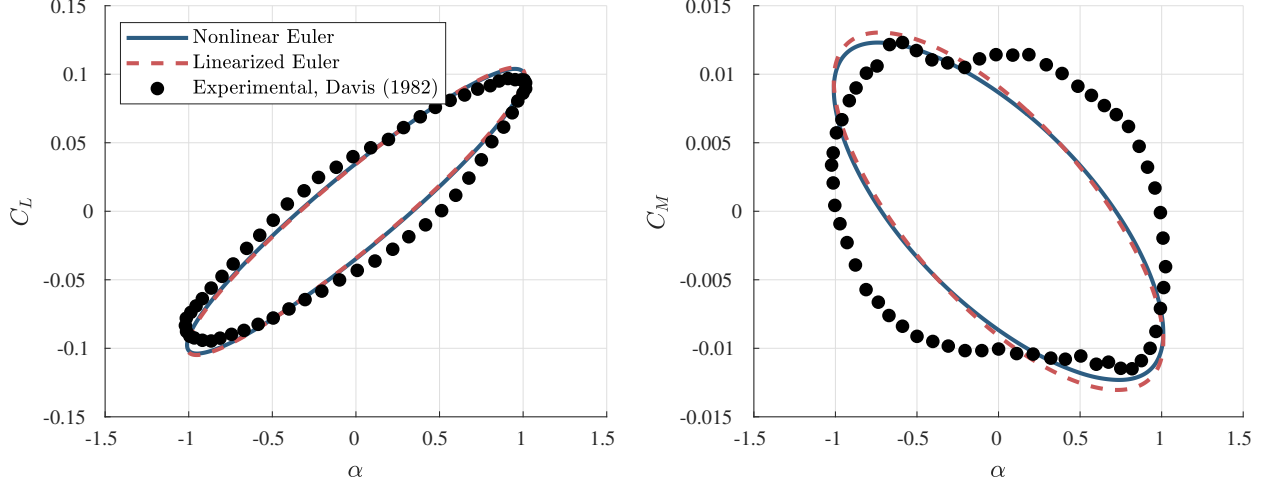


Fig. 2 C_l (left) and C_m (right) versus angle of attack for the nonlinear and linearized Euler equations, and experimental results obtained by Davis [40].

B. Full-Order Flutter Predictions

As the results for the ROM-based flutter predictions are compared to the full-order model predictions, the methodology used to obtain a flutter boundary using the full-order model is first outlined. The methodology used is based on the one described by Edwards *et al.* [42]. In this approach, the structural model (23) is marched in time with the following method,

$$\mathbf{u}_s^{(n+1)} = \exp(A_s \Delta t) \mathbf{u}_s^{(n)} + \left[\int_0^{\Delta t} \exp(A_s (\Delta t - \tau)) d\tau \right] \mathbf{f}_s^{(n)} \quad (37)$$

where Δt is the time step size, and n is the step index. For each time step, the aerodynamic forces are first computed using either the nonlinear or the linearized Euler equations marched in time using the implicit Euler method. These forces are transferred to the structural model, which then determines the structural deformation. Deformations are transferred to the aerodynamic mesh, and computations are repeated until the aerodynamic forces have converged to a relative tolerance of $O(10^{-6})$ between iterations. Typically, four iterations are required to complete one step in time.

In order to determine the flutter boundary using the full-order nonlinear and linearized Euler equations, at least two-simulations are required: one below the flutter boundary, and one above. Time histories of the aeroelastic transients are fit to a damped sinusoidal wave using the methodology of Bennett and Desmarais [43]. This allows for a damping factor to be obtained for each dynamic pressure of interest, allowing for the flutter boundary to be interpolated as the point of zero damping. It is important to note that the time-marched aeroelastic simulations were not optimized to reduce computational expense.

C. Two Degree of Freedom Aeroelastic Test Case

To test the accuracy of the proposed approach for fast flutter predictions, the two degree of freedom airfoil structure shown in Figure 3 has been implemented. The structure is supported by a torsional and a linear spring and is capable of both pitching and plunging. For the equations of motion presented in (21) and (22), the quantities for this model are:

$$\mathbf{M} = \begin{bmatrix} 1 & x_\alpha \\ x_\alpha & r_\alpha^2 \end{bmatrix}, \quad \mathbf{K} = \begin{bmatrix} (\omega_h/\omega_\alpha)^2 & 0 \\ 0 & r_\alpha^2 \end{bmatrix}, \quad \mathbf{f} = \begin{bmatrix} -C_l \\ 2C_m \end{bmatrix},$$

where x_α is the distance from the elastic axis to the centre of gravity (divided by b), r_α is the radius of gyration (divided by b), and ω_h and ω_α are the uncoupled plunging and pitching natural frequencies, respectively. C_m is taken about the elastic axis location. Aeroelastic results are presented for Case A of Isogai [44]. Parameter values used are: $a = -2.0$, $x_\alpha = 1.8$, $r_\alpha = 1.865$, $\omega_h = 100$ rad/s, $\omega_\alpha = 100$ rad/s, and $\mu = 60$. Note that this value of a corresponds to an elastic axis location ahead of the leading edge; this replicates the behaviours of a swept back wing. Flutter predictions are performed about a steady state angle of attack of 0° .

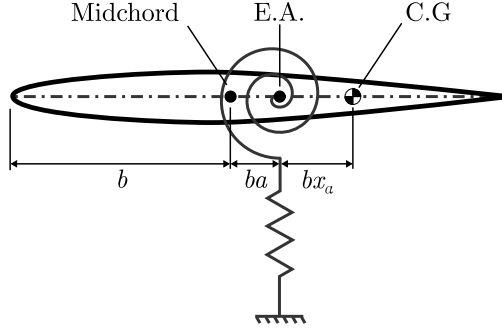


Fig. 3 Two degree of freedom airfoil structure capable of pitching and plunging.

Table 1 Total time required to obtain the flutter boundary for all Mach numbers of interest, measured in equivalent number of steady flow solves.

	Nonlinear Euler	Linearized Euler	ROM
Total Time [equivalent number of steady solves]	1751	783	58

1. Full-Order and Reduced-Order Models

Simulations were performed on the NACA 64A010 airfoil with a structured O-mesh. The mesh consists of a two-dimensional mesh with 38,000 nodes around the airfoil extruded to create 11 span-wise sections, resulting in a total of 418,000 nodes subdivided into 32 blocks. All results and snapshots were obtained on 32 Intel "Skylake" processors at 2.4 GHz.

The aerodynamic ROMs used for this test case were constructed using the procedure outlined in Section III. Through experimentation, it was found that 2000 snapshots for each Mach number with a time step size of 0.15 resulted in ROMs capable of accurate flutter predictions. Using the POD-based approach, the ROMs were constructed for a number of Mach numbers ranging from 0.75 to 0.875, each with approximately 150 degrees of freedom obtained using a tolerance $\eta = 10^{-8}$ from equation (16). This reduction in dimension is significant compared to the 2.09×10^6 degrees of freedom in the original system.

2. Flutter Predictions

Results for the flutter boundary obtained by the nonlinear and linearized Euler equations, the ROM, and those found in the literature are shown in Figure 4. Results from Alonso and Jameson [45] were obtained using the Euler equations, while Sanchez *et al.* [46] used the Reynolds-Average Navier-Stokes (RANS) equations. All methods used in the present work have good agreement with the results from the literature for all Mach numbers. The transonic dip around Mach 0.85 is observed in the results. This is the result of nonlinear behaviour in the flow field, specifically the oscillation of the shock wave on the upper surface [44]. This indicates that the ROM is capable of capturing this nonlinear flow behaviour, which would not be captured by a linear aerodynamic method. Additionally, one observes two points at Mach 0.875: an onset of flutter at $V_f \approx 0.6$, and the return of stability at $V_f \approx 1.8$. Of these two points, the ROM predicts the former well, but is incapable of predicting the latter. Moreover, the ROM does exhibit some deviations from the results of the other methods at the lower Mach numbers. Both of these discrepancies may be correctable with modifications to the method of snapshot collection, for example by increasing the number of snapshots.

A comparison of the total time (measured in equivalent number of steady flow solves) required to obtain the flutter boundary for all Mach numbers is presented in Table 1. As expected, the nonlinear and linearized Euler equations require significantly more time than the ROM. However, as mentioned above, the methodology used to obtain the flutter boundary for the full-order models was not optimized for computational time, and further reduction in these times may be expected. Despite these caveats, the use of the ROM for flutter prediction performed considerably faster. Notably, most of the time for the ROM was in collecting the snapshots for basis construction. On average, 92.1% of the time was required to collect the snapshots and construct the reduced basis, 7.77% was required for the steady flow solve, while only 0.134% was required to perform the eigenvalue analyses of the monolithic system at all values of V_f .

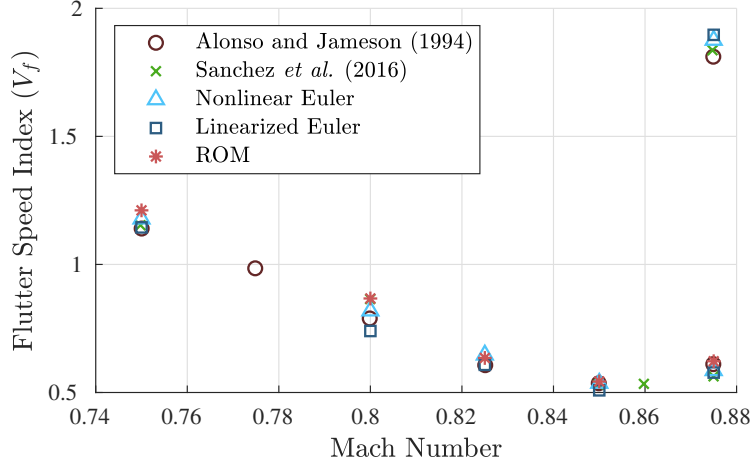


Fig. 4 Flutter boundary obtained by Alonso and Jameson [45] and Sanchez *et al.* [46], by the nonlinear and linearized Euler equations, and by the ROM-based approach.

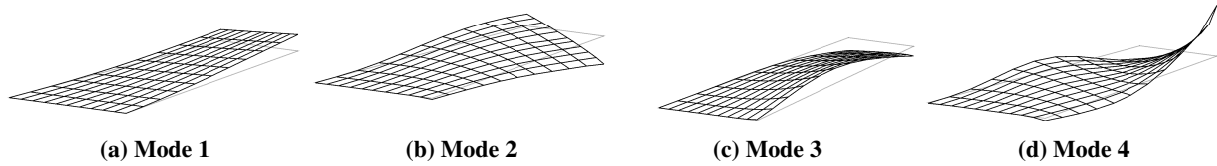


Fig. 5 First four mode shapes of the AGARD 445.6 wing structure.

D. AGARD Wing Aeroelastic Test Case

As a three-dimensional aeroelastic test case, the weakened AGARD 445.6 wing model was chosen, for which wind tunnel results were obtained by Yates [47]. The structural model provided in [47] is composed of four natural frequencies and associated mode shapes, the latter shown in Figure 5. Both time history results and a flutter boundary prediction obtained by the ROM are presented below. Results are compared to those obtained by the full-order linearized discrete Euler equations.

1. Full-Order and Reduced-Order Models

Simulations were performed on the AGARD 445.6 wing geometry using a structured H-C mesh with 1,987,392 nodes subdivided into 160 blocks. All results and snapshots were obtained on 160 Intel "Skylake" processors at 2.4 GHz.

The aerodynamic ROMs used for the AGARD 445.6 wing were constructed using the procedure outlined in Section III. It was determined through experimentation that 3000 snapshots for each Mach number with a time step size of 2.0 produced accurate ROMs. Using the POD-based approach, the ROMs were constructed for various Mach numbers ranging from 0.499 to 1.141, each with approximately 220 degrees of freedom obtained using $\eta = 10^{-8}$.

2. Time History and Flutter Predictions

To demonstrate the accuracy of the aerodynamic ROM, Figure 6 shows the time history of the generalized coordinates of the AGARD wing coupled to both the full-order linearized Euler equations and the ROM, subject to an initial velocity perturbation. From this figure, it is observed that the ROM is capable of producing similar aeroelastic transients. The damping factor for each of the displacements is well captured, indicating that instabilities in the aeroelastic system are reproducible with the ROM. However, the shift in the solution at later times indicates that the exact flow solution for this structural displacement time history does not exist in the reduced basis used to create the ROM. Indeed, unless the exact time history of the generalized coordinates is known *a priori* (in which case we would not require the ROM) or all possible flow field reactions are captured (which would lead to high computational costs), the ROM's solution will always remain an approximation of its full-order counterpart. A better approximation can be obtained by using more snapshots to create the reduced basis; however this comes at an increased computational cost.

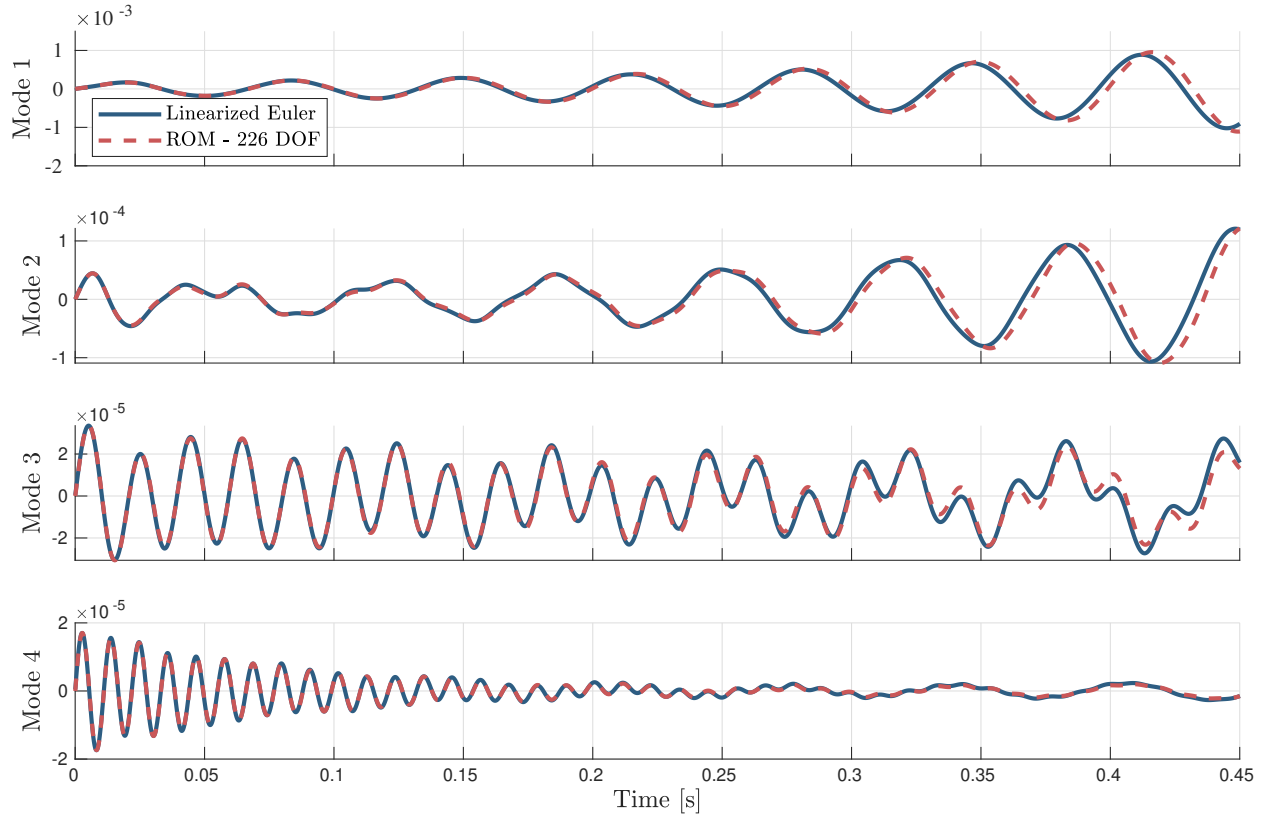


Fig. 6 Generalized structural coordinate displacements obtained by both the linearized Euler equations and the ROM for the AGARD 445.6 wing at a Mach number of 0.960 and dynamic pressure of 0.57 psi.

Further comparison between the ROM and the full-order linearized Euler results is provided by looking at the frequency spectrum shown in Figure 7, obtained by performing a fast-Fourier transform of the time histories from Figure 6. It is observed that the frequency peaks in the solution are generally well captured by the ROM. Ultimately, the behaviour of the ROM is heavily reliant on the snapshots used to create the reduced basis. As described in Section III, each mode shape was excited using filtered noise to create the flow field snapshots. The idea for the use of the low-pass filter with a cutoff frequency tuned to each mode's natural frequency was initially conceived by analyzing frequency spectrum plots such as Figure 7. Looking at both Figures 6 and 7, it is seen that each generalized coordinate tends to initially oscillate at a frequency close to its natural frequency before coupling to a dominant lower frequency in the system. In the case of the first mode, these peaks coalesce to produce a single dominant frequency. Using the low-pass filter to create the structural excitations for the snapshots allows for the flow field's response to be captured for a combination of structural frequencies below the natural frequency of each mode. This seems to provide adequately relevant flow field snapshots for the behaviour of the structure close to the flutter boundary. Further investigation is required to determine if this technique remains appropriate for structural models with more than four modes.

Results for the flutter boundary obtained for the AGARD wing are shown in Figure 8, from which several observations can be made. First, as observed by Lee-Rausch and Batina [48], the inclusion of viscosity in the solution is important for predicting accurate flutter behaviour at Mach numbers close to unity. Indeed, the current ROM-based approach is not limited to inviscid equations and can be extended to the linearized discrete RANS equations. Second, the flutter boundary obtained by the linearized Euler equations has similar behaviour as the nonlinear inviscid results obtained by Silva *et al.* [49], but does not correspond exactly. This may be due to a number of factors, including time step size and grid resolution; further investigation is required. Finally, it is observed that the ROM-based approach demonstrates similar accuracy as the linearized Euler equations for all Mach numbers of interest, save Mach 1.141. Thus, in general the ROM shows an ability to closely mimic the governing equations from which it is derived.

The behaviour of an aerodynamic ROM for the prediction of flutter for the AGARD wing at Mach 1.141 has been previously analyzed by Silva *et al.* [49]. With the use of the root locus plot of the aeroelastic system, Silva *et al.*

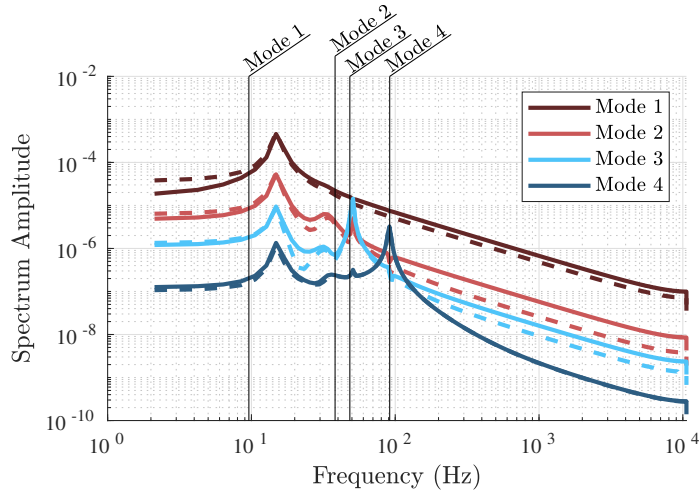


Fig. 7 Frequency spectrum of the time history response for the AGARD wing shown in Figure 6; solid lines are the full-order model, dashed lines are the ROM, black vertical lines indicate the natural frequency for each mode.

Table 2 Total time required to obtain the flutter boundary for the AGARD wing for all Mach numbers, measured in equivalent number of steady flow solves.

	Linearized Euler	ROM
Total Time [equivalent number of steady solves]	1101	263

concluded that for the ROM constructed based on the Euler equations at this Mach number, the third structural mode demonstrated instabilities at all dynamic pressures. In the present work, instabilities were observed at dynamic pressures above 0.5 psi, well below those predicted by the full-order linearized Euler equations. This instability is difficult to capture using the time-marched aeroelastic transients due to the high frequency content of the third mode’s response, making it difficult to fit with a damped sinusoidal wave. At lower Mach numbers, the first mode demonstrates the aeroelastic instability; it is thus assumed that at Mach 1.141, this mode will also be responsible for flutter. The third mode’s transients are stabilized with the inclusion of viscosity, i.e. with the use of the RANS equations [49]. Ultimately, it can be concluded that the use of the Euler equations is inappropriate for determining the flutter boundary of the AGARD wing at Mach 1.141.

Table 2 shows the total time required to obtain the flutter boundary for all Mach numbers of interest, measured in terms of the equivalent number of steady flow solves. As is expected, the use of the ROM for flutter predictions is considerably faster than the full-order linearized discrete Euler equations. The total time reported in Table 2 for the linearized Euler equations assumes the best case scenario for which only two simulations are required: one at a dynamic pressure below the flutter boundary and one above. However, with aircraft for which flutter behaviour is not known *a priori*, increased computational costs can be anticipated because the aeroelastic transients may be required for more than two dynamic pressures. Comparatively, the aerodynamic ROM is nondimensionalized with respect to the dynamic pressure, and thus a sweep across multiple values is extremely rapid.

VI. Conclusions

This paper presents a methodology for flutter predictions using a POD-based model order reduction approach. The resulting aerodynamic ROMs are of sufficiently low order that the determination of a flutter boundary can be cast as an eigenvalue problem. The concepts presented herein have been shown to be effective for predicting the flutter boundary of a two degree of freedom airfoil structure and the three-dimensional AGARD 445.6 wing for most Mach numbers. Significant time reductions are obtained compared to the full-order flutter prediction methodology. Due to the inaccuracies demonstrated by the Euler equations for the AGARD wing flutter boundary at higher Mach numbers, the

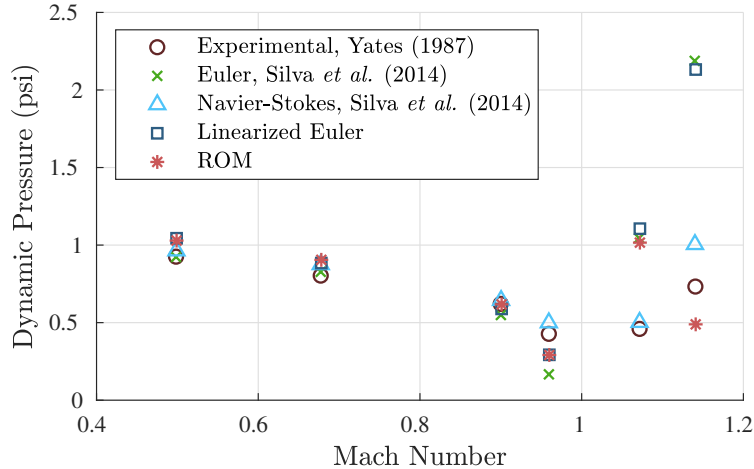


Fig. 8 Flutter boundary for the AGARD 445.6 wing obtained experimentally by Yates [47], computationally by Silva *et al.* [49], by the linearized discrete Euler equations, and by the current ROM approach.

use of the RANS equations to construct the aerodynamic ROMs would lead to more reliable results. The implementation of this algorithm for fast flutter prediction is a step towards including a flutter constraint for an aircraft optimization framework.

Acknowledgements

This research was enabled in part by the financial support provided by Bombardier, the Government of Ontario, the Natural Sciences and Research Council of Canada, and the University of Toronto. Computational resources were provided by SciNet HPC Consortium, a part of Compute Canada. The authors are extremely grateful for the input and support provided by Professor Masayuki Yano.

References

- [1] Hicken, J. E., and Zingg, D. W., "Aerodynamic Optimization Algorithm with Integrated Geometry Parameterization and Mesh Movement," *AIAA Journal*, Vol. 48, No. 2, 2010, pp. 400–413.
- [2] Osusky, L., Buckley, H., Reist, T., and Zingg, D. W., "Drag Minimization Based on the Navier–Stokes Equations Using a Newton–Krylov Approach," *AIAA Journal*, Vol. 53, No. 6, 2015, pp. 1555–1577.
- [3] Reist, T. A., and Zingg, D. W., "High-Fidelity Aerodynamic Shape Optimization of a Lifting-Fuselage Concept for Regional Aircraft," *Journal of Aircraft*, Vol. 54, No. 3, 2016, pp. 1085–1097.
- [4] Zhang, Z. J., and Zingg, D. W., "Efficient Monolithic Solution Algorithm for High-Fidelity Aerostructural Analysis and Optimization," *AIAA Journal*, Vol. 56, No. 3, 2018, pp. 1251–1265.
- [5] Mallik, W., Kapania, R. K., and Schetz, J. A., "Effect of Flutter on the Multidisciplinary Design Optimization of Truss-Braced-Wing Aircraft," *Journal of Aircraft*, Vol. 52, No. 6, 2015, pp. 1858–1872.
- [6] Theodorsen, T., "General Theory of Aerodynamic Instability and the Mechanism of Flutter," Tech. Rep. 496, National Advisory Committee for Aeronautics, 1949.
- [7] Jonsson, E., Mader, C. A., Kennedy, G., and Martins, J., "Computational Modeling of Flutter Constraint for High-Fidelity Aerostructural Optimization," *AIAA Scitech 2019 Forum*, San Diego, California, 2019, AIAA 2019-2354.
- [8] Lupp, C. A., and Cesnik, C. E., "A Gradient-Based Flutter Constraint Including Geometrically Nonlinear Deformations," *AIAA Scitech 2019 Forum*, San Diego, California, 2019, AIAA 2019-1212.
- [9] Opgenoord, M. M. J., Drela, M., and Willcox, K. E., "Influence of Transonic Flutter on the Conceptual Design of Next-Generation Transport Aircraft," *AIAA Journal*, Vol. 57, No. 5, 2019, pp. 1973–1987.

- [10] Jacobson, K. E., Kiviahio, J. F., Kennedy, G. J., and Smith, M. J., “Evaluation of Time-Domain Damping Identification Methods for Flutter-Constrained Optimization,” *Journal of Fluids and Structures*, Vol. 87, 2019, pp. 174–188.
- [11] Jonsson, E., Riso, C., Lupp, C. A., Cesnik, C. E., Martins, J. R., and Epureanu, B. I., “Flutter and post-flutter constraints in aircraft design optimization,” *Progress in Aerospace Sciences*, Vol. 109, 2019.
- [12] Bendiksen, O. O., “Review of Unsteady Transonic Aerodynamics: Theory and Applications,” *Progress in Aerospace Sciences*, Vol. 47, No. 2, 2011, pp. 135–167.
- [13] Henshaw, M., Badcock, K., Vio, G., Allen, C., Chamberlain, J., Kaynes, I., Dimitriadis, G., Cooper, J., Woodgate, M., Rampurawala, A., Jones, D., Fenwick, C., Gaitonde, A., Taylor, N., Amor, D., Eccles, T., and Denley, C., “Non-Linear Aeroelastic Prediction for Aircraft Applications,” *Progress in Aerospace Sciences*, Vol. 43, No. 4, 2007, pp. 65–137.
- [14] Thomas, J. P., Dowell, E. H., and Hall, K. C., “Three-Dimensional Transonic Aeroelasticity Using Proper Orthogonal Decomposition-Based Reduced-Order Models,” *Journal of Aircraft*, Vol. 40, No. 3, 2003, pp. 544–551.
- [15] Beran, P. S., Lucia, D. J., and Pettit, C. L., “Reduced-Order Modelling of Limit-Cycle Oscillation for Aeroelastic Systems,” *Journal of Fluids and Structures*, Vol. 19, No. 5, 2004, pp. 575–590.
- [16] Anttonen, J. S., King, P. I., and Beran, P. S., “Applications of multi-POD to a pitching and plunging airfoil,” *Mathematical and Computer Modelling*, Vol. 42, No. 3, 2005, pp. 245–259.
- [17] Lieu, T., Farhat, C., and Lesoinne, M., “Reduced-Order Fluid/Structure Modeling of a Complete Aircraft Configuration,” *Computer Methods in Applied Mechanics and Engineering*, Vol. 195, No. 41, 2006, pp. 5730–5742.
- [18] Lieu, T., and Farhat, C., “Adaptation of Aeroelastic Reduced-Order Models and Application to An F-16 Configuration,” *AIAA Journal*, Vol. 45, No. 6, 2007, pp. 1244–1257.
- [19] Amsallem, D., Tezaur, R., and Farhat, C., “Real-Time Solution of Linear Computational Problems Using Databases of Parametric Reduced-Order Models with Arbitrary Underlying Meshes,” *Journal of Computational Physics*, Vol. 326, 2016, pp. 373–397.
- [20] Zhang, W., Wang, B., Ye, Z., and Quan, J., “Efficient Method for Limit Cycle Flutter Analysis Based on Nonlinear Aerodynamic Reduced-Order Models,” *AIAA Journal*, Vol. 50, No. 5, 2012, pp. 1019–1028.
- [21] Kou, J., and Zhang, W., “A Hybrid Reduced-Order Framework for Complex Aeroelastic Simulations,” *Aerospace Science and Technology*, Vol. 84, 2019, pp. 880 – 894.
- [22] Waite, J., Stanford, B., Bartels, R. E., and Silva, W. A., “Reduced Order Modeling for Transonic Aeroservoelastic Control Law Development,” *AIAA Scitech 2019 Forum*, San Diego, California, 2019, AIAA 2019-1022.
- [23] Silva, W., “AEROM: NASA’s Unsteady Aerodynamic and Aeroelastic Reduced-Order Modeling Software,” *Aerospace*, Vol. 5, No. 2, 2018, pp. 41–58.
- [24] Dongfeng, L., Chen, G., Li, Y., and Da Ronch, A., “Transonic Aeroelastic Global Structural Optimization using an Efficient CFD-based Reduced Order Model with Flutter Constraints,” *AIAA Scitech 2019 Forum*, San Diego, California, 2019, AIAA 2019-1700.
- [25] Hicken, J. E., and Zingg, D. W., “Parallel Newton-Krylov Solver for the Euler Equations Discretized Using Simultaneous Approximation Terms,” *AIAA Journal*, Vol. 46, No. 11, 2008, pp. 2773–2786.
- [26] Hicken, J. E., Osusky, M., and Zingg, D. W., “Comparison of Parallel Preconditioners for a Newton-Krylov Flow Solver,” *Computational Fluid Dynamics 2010*, Springer Berlin Heidelberg, Berlin, Heidelberg, 2011, pp. 457–463.
- [27] Kreiselmaier, E., and Laschka, B., “Small Disturbance Euler Equations: Efficient and Accurate Tool for Unsteady Load Prediction,” *Journal of Aircraft*, Vol. 37, No. 5, 2000, pp. 770–778.
- [28] Thomas, P., and Lombard, C., “Geometric Conservation Law and Its Application to Flow Computations on Moving Grids,” *AIAA Journal*, Vol. 17, No. 10, 1979, pp. 1030–1037.
- [29] Leung, T. M., and Zingg, D. W., “Aerodynamic Shape Optimization of Wings Using a Parallel Newton-Krylov Approach,” *AIAA Journal*, Vol. 50, No. 3, 2012, pp. 540–550.
- [30] Hicken, J. E., and Zingg, D. W., “A Simplified and Flexible Variant of GCROT for Solving Nonsymmetric Linear Systems,” *SIAM Journal on Scientific Computing*, Vol. 32, No. 3, 2010, pp. 1672–1694.

- [31] Benner, P., Gugercin, S., and Willcox, K., “A Survey of Projection-Based Model Reduction Methods for Parametric Dynamical Systems,” *SIAM Review*, Vol. 57, No. 4, 2015, pp. 483–531.
- [32] Volkwein, S., *Proper Orthogonal Decomposition: Theory and Reduced-Order Modelling*, Lecture Notes, University of Konstanz, Konstanz, Germany, 2013.
- [33] Holmes, P., Lumley, J. L., Berkooz, G., and Rowley, C. W., *Turbulence, Coherent Structures, Dynamical Systems and Symmetry*, Cambridge University Press, Cambridge, UK, 1996.
- [34] Bishop, C. M., *Pattern Recognition and Machine Learning*, Springer Science+Business Media, New York, USA, 2006.
- [35] Kalashnikova, I., Barone, M. F., Arunajatesan, S., and van Bloemen Waanders, B. G., “Construction of energy-stable projection-based reduced order models,” *Applied Mathematics and Computation*, Vol. 249, 2014, pp. 569–596.
- [36] Kim, T., Hong, M., Bhatia, K. G., and SenGupta, G., “Aeroelastic model reduction for affordable computational fluid dynamics-based flutter analysis,” *AIAA Journal*, Vol. 43, No. 12, 2005, pp. 2487–2495.
- [37] Silva, W. A., “Simultaneous Excitation of Multiple-Input/Multiple-Output CFD-Based Unsteady Aerodynamic Systems,” *Journal of Aircraft*, Vol. 45, No. 4, 2008, pp. 1267–1274.
- [38] Dowell, E. H., Peters, D. A., Clark, R., Scanlan, R., Cox, D., Simiu, E., Curtiss, H. J., Sisto, F., Edwards, J. W., and Hall, K. C., *A Modern Course in Aeroelasticity*, 4th ed., Kluwer Academic Publishers, New York, USA, 2004.
- [39] Rendall, T., and Allen, C., “Unified Fluid–Structure Interpolation and Mesh Motion Using Radial Basis Functions,” *International Journal for Numerical Methods in Engineering*, Vol. 74, No. 10, 2008, pp. 1519–1559.
- [40] AGARD, “Compendium of Unsteady Aerodynamic Measurements,” Tech. Rep. 702, Advisory Group for Aerospace Research and Development (AGARD), 1982.
- [41] Chyu, W., Davis, S., and Chang, K. S., “Calculation of Unsteady Transonic Flow Over An Airfoil,” *AIAA Journal*, Vol. 19, No. 6, 1981, pp. 684–690.
- [42] Edwards, J. W., Bennett, R. M., Whitlow, W., and Seidel, D. A., “Time-Marching Transonic Flutter Solutions Including Angle-Of-Attack Effects,” *Journal of Aircraft*, Vol. 20, No. 11, 1983, pp. 899–906.
- [43] Bennett, R. M., and Desmarais, R. N., “Curve fitting of aeroelastic transient response data with exponential functions,” Tech. rep., National Aeronautics and Space Administration, 1976.
- [44] Isogai, K., “Numerical Study of Transonic Flutter of a Two-Dimensional Airfoil,” Tech. Rep. TR-617T, National Aerospace Laboratory, July 1980.
- [45] Alonso, J., and Jameson, A., “Fully-Implicit Time-Marching Aeroelastic Solutions,” *32nd Aerospace Sciences Meeting and Exhibit*, Reno, Nevada, 1994, AIAA 1994-56.
- [46] Sanchez, R., Kline, H., Thomas, D., Variyar, A., Righi, M., Economon, T. D., Alonso, J. J., Palacios, R., Dimitriadis, G., and Terrapon, V., “Assessment of the fluid-structure interaction capabilities for aeronautical applications of the open-source solver SU2,” *ECCOMAS Congress 2016 - Proceedings of the 7th European Congress on Computational Methods in Applied Sciences and Engineering*, Crete Island, Greece, 2016, pp. 1498–1529.
- [47] Yates Jr, E. C., “AGARD Standard Aeroelastic Configurations for Dynamic Response. Candidate Configuration I.-Wing 445.6,” Tech. Rep. N88-11202, National Aeronautics and Space Administration, 1987.
- [48] Lee-Rausch, E., and Batina, J., “Calculation of AGARD Wing 445.6 flutter using Navier-Stokes aerodynamics,” *11th Applied Aerodynamics Conference*, Monterey, California, 1993, AIAA 1993-3476.
- [49] Silva, W. A., Chwalowski, P., and Perry III, B., “Evaluation of linear, inviscid, viscous, and reduced-order modelling aeroelastic solutions of the AGARD 445.6 wing using root locus analysis,” *International Journal of Computational Fluid Dynamics*, Vol. 28, No. 3-4, 2014, pp. 122–139.